

GIGAS: a set of microwave sensor arrays to detect molecular bremsstrahlung radiation from extensive air shower

R. Gaïor^{a,*}, I. Al Samarai^{a,b,1}, C. Bérat^c, M. Blanco Otano^a, J. David^a, O. Deligny^b,
H. Lebbolo^a, S. Lecoq^{c,2}, A. Letessier-Selvon^a, I. Lhenry-Yvon^b, I. C. Mariş^{a,3},
F. Montanet^c, P. Repain^a, F. Salamida^{b,4}, M. Settimo^{a,5}, P. Stassi^c, A. Stutz^c

^a*Laboratoire de Physique Nucléaire et de Hautes Energies (LPNHE), Universités Paris 6 et Paris 7, CNRS-IN2P3, Paris, France*

^b*Institut de Physique Nucléaire d'Orsay (IPNO), Université Paris 11, CNRS-IN2P3, France*

^c*Laboratoire de Physique Subatomique et de Cosmologie (LPSC), Université Grenoble-Alpes, CNRS-IN2P3, France*

Abstract

We present the GIGAS (Gigahertz Identification of Giant Air Shower) microwave radio sensor arrays of the EASIER project (Extensive Air Shower Identification with Electron Radiometers), deployed at the site of the Pierre Auger cosmic ray observatory. The aim of these novel arrays is to probe the intensity of the molecular bremsstrahlung radiation expected from the development of the extensive air showers produced by the interaction of ultra high energy cosmic rays in the atmosphere. In the designed setup, the sensors are embedded within the surface detector array of the Pierre Auger observatory allowing us to use the particle signals at ground level to trigger the radio system. A series of seven, then 61 sensors have been deployed in the C-band, followed by a new series of 14 higher sensitivity ones in the C-band and the L-band. The design, the operation, the calibration and the sensitivity to extensive air showers of these arrays are described in this paper.

Keywords: high energy cosmic rays, microwave, radio, molecular bremsstrahlung

*Corresponding author

Email address: romain.gaïor@lpnhe.in2p3.fr (R. Gaïor)

¹Now at DPNC Université de Genève, Switzerland

²Now at National Astronomical Observatory, Chinese Academy of Sciences, Beijing 100012, China

³Now at Université Libre de Bruxelles (ULB), Brussels, Belgium

⁴Università dell'Aquila, Dipartimento di Scienze Fisiche e Chimiche, L'Aquila, Italy

⁵Now at SUBATECH, Université de Nantes, Ecole des Mines de Nantes, CNRS-IN2P3, Nantes, France

1. Introduction

The very low flux of Ultra High Energy Cosmic Rays (UHECRs), less than one particle per year per square kilometers above 10^{19} eV, requires a very large detection surface at ground level to measure the primary particle properties via the Extensive Air Showers (EAS) they produce in the atmosphere. Such an indirect measurement is a very difficult technical challenge and the search for efficient but low cost techniques is an ongoing process.

As of today, the largest cosmic ray observatories, the Pierre Auger Observatory [1] and Telescope Array [2], combine two techniques to measure EAS: an array of particle detectors at ground supplemented by a network of fluorescence telescopes overlooking the atmosphere above the ground array. The particle detectors, scintillators or water Cherenkov detectors, sample the lateral profile of the cascades that reach the ground, while the telescopes measure the longitudinal profile of the cascades by detecting the fluorescence light emitted isotropically by the nitrogen atoms previously excited by the passage of the electromagnetic component of the EAS. While extremely powerful, the combination of these two techniques suffers from the limited duty cycle, less than 15%, of the fluorescence technique, which can only be active during clear moonless nights. With such a limited duty cycle, the mass composition information, best determined by the depth of the maximum of the longitudinal profiles, is essentially unavailable for UHECRs with energies above $\simeq 4 \times 10^{19}$ eV. As such, the question of the origin and nature of UHECR in this energy range, where a strong flux suppression has been measured in the energy spectrum, remains unsolved. Indeed, the interpretation of this cut-off is still being debated [3].

One of the main motivation for using the radio emission of EAS to measure UHECR properties relies on its capabilities to provide similar information as the fluorescence technique but without the duty cycle limitation. Initially proposed and implemented in the 1960's [4], the radio detection of EAS is now a well-established technique and has been mostly exploited in the VHF band [5–7] and [8] for a recent review. In this frequency range, the observed radiation is mainly produced by the acceleration of the electrons of the shower in the geomagnetic field, and, to a smaller extent, by the moving charge excess (also known as Askaryan radiation) [9]. However, both of these radiations are beamed forward in the Cherenkov cone, which is around $\simeq 1^\circ$ in air, and centered around the shower axis. The resulting imprint of the radio signal at ground level is generally observable only up to a few hundred meters, limiting this technique to densely-instrumented arrays. Although such densely-instrumented arrays can be deployed over surfaces that provide good sensitivity to study cosmic rays with primary energies of about 10^{18} eV or less, the cost is then a limiting factor to envisage the deployment of antennas over the surfaces needed to probe the flux at the highest energies. In addition, the collimated emission of the radiation limits the ability to measure the longitudinal development of the showers as one only detects the ground projection of this profile around the shower axis.

In 2008, an accelerator experiment, SLAC T471, detected a signal in the microwave

frequency range (1.5-6 GHz) upon the passage of an electromagnetic shower in an anechoic chamber [10]. This signal was interpreted as Molecular Bremsstrahlung Radiation (MBR), and its intensity, extrapolated to UHECR energies, was then expected to be detectable with rather simple radio-detector systems. The MBR is produced by the acceleration of the ionization electrons in the electric field of the atmosphere molecules. The radiation is in principle isotropic and its intensity directly related to the energy deposited by the EAS particles in the atmosphere. MBR profiles would therefore be very similar to fluorescence ones, with the advantage that MBR detection in the microwave band, where the atmosphere is essentially transparent, can be done with a 100% duty cycle. Such a promising signal, together with the fact that sensors in that band are very cheap due to their commercial use for satellite TV reception, led to the development of additional accelerator experiments to better characterize the signal [11], [12]. In addition, several in situ experiments aiming at the direct observation of the MBR emission from EAS like MIDAS [13], CROME [14], AMBER [15] and EASIER were also set up.

The combined measurements of the EAS longitudinal profile in the atmosphere and of the particle contents at ground allow the reconstruction of the shower key parameters and thus a better understanding of the mass of UHECRs. For a large enough MBR signal, the EASIER setup, which is presented in this paper, was designed to allow an access to several composition indicators such as the shower depth of maximum and the muonic-to-electromagnetic ratio on an event by event basis. This information would help to understand whether the suppression observed in the energy spectrum is the result of the extinction of the sources (i.e. the acceleration mechanisms has reached its maximum potential) or the result of a propagation effect, due to the interaction of UHECRs with the cosmic microwave background of radiation (the Greisen, Zatsepin and Kuzmin (GZK) cut-off [16, 17]).

In this paper, we present the developments of the EASIER project, a concept of radio detectors integrated to the Surface Detector (SD) of the Pierre Auger Observatory. An EASIER detector is a radio antenna combined with an envelope detector integrated to an SD station. EASIER thus take advantage of the power supply and data acquisition but takes most of its benefits from the station trigger. Radio Frequency Interference (RFI) and especially the anthropogenic noises are by this mean filtered out. Thus, this setup has the capability to probe the radio signal from UHECRs at large distances from the shower axis. In section 2, the general concept of EASIER is first presented prior the description of the three different versions of microwave sensor arrays installed in the GHz frequencies: GIGAS61, GIGADuck-C and GIGADuck-L. The full calibration of these detectors is then detailed in section 3. Finally the method to simulate the MBR is described and combined to the calibration information to produce estimations of the systems sensitivity in section 4.

2. The EASIER detection setup, GIGAS61 and GIGADuck detectors

EASIER is a novel radio-detector concept composed of a radio sensor and of an envelope detection electronics embedded in the SD of the Pierre Auger Observatory. This concept was implemented in three bandwidths: the VHF band (30-80 MHz), the L band (1-1.5 GHz) and the C-band (3.4-4.2 GHz). We focus in this article on the L- and C-band only. The EASIER experiment is one of the three experiments deployed at the Pierre Auger Observatory to search for the MBR emitted by the ionization electrons left in the atmosphere after the passage of the shower. In contrast to the two other ones, namely AMBER [15] and MIDAS [13], which instrument an array of feed horn antennas illuminated by a parabolic dish, EASIER relies on the observation of the shower from the ground level with a wide angle antenna pointing directly to the sky. In 2011, a first set of 7 antennas was deployed, followed by 54 additional in 2012 making the GIGAS61 array. The analysis of GIGAS61 data has revealed the observation of radio signals emitted by EAS in the C-band [15]. However, such detection occurred only for air showers at distances less than around 200 m from the GIGAS61 antenna and could be also explained by other emission processes than the MBR. Furthermore, new estimations of the expected MBR intensity [18, 19] led to the development of two new versions of EASIER, called GIGADuck-C (installed in March 2015) and GIGADuck-L (installed in December 2016), with an enhanced sensitivity to search for signal from larger distances hence fainter.

2.1. The electromagnetic background at the Pierre Auger Observatory

Radio measurement are often hindered by man-made noise. Prior to the installation, the electromagnetic background was measured on the site of the Pierre Auger Observatory located in the Pampa Amarilla in the province of Mendoza in Argentina. Figure 1 shows the power spectrum between 2.6 and 4.6 GHz measured with a C-band LNBF (Low Noise Block feed). The gain of the amplifier used is roughly 60 dB between 3.4 and 4.2 GHz. With a recorded power in the sensitive bandwidth of -55 dBm / 3MHz the noise floor is thus about -180 dBm/Hz. No strong peak is observed above this level in the tens of recorded spectra making this band adequate for our experiment. In the L-band (see Figure 1 (right)), peaks can be noticed, in particular around 900 MHz where a strong intermittent peak could be observed. It originates from the Auger SD communication system and the mobile phone band and can be reduced with an appropriate filtering. Other peaks are also present inside the frequency band of interest between 1 and 1.4 GHz but their amplitude remains acceptable.

2.2. The experimental setup

The EASIER detector is embedded in a sub-array of the surface detector (SD) of the Pierre Auger Observatory. The SD is composed of 1660 water Cherenkov detectors (WCD) arranged in a triangular grid of 1500 m spacing. Each WCD is equipped with three Photo Multiplier Tubes (PMT), a local acquisition and a communication system, see [1] for a detailed description. An EASIER detector unit is designed to be integrated into a WCD. It is composed radio sensor installed on top of the SD station and an electronics box located below the hatch box on top of the SD electronics (see Fig. 3). The three setups described in this paper share common elements presented rightafter, their

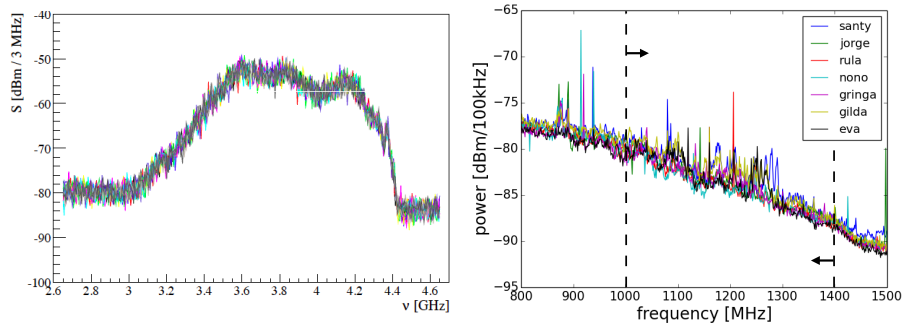


Figure 1: Frequency spectra in Pampa Amarilla in the C-band recorded (left) and in the L-band (right). The band between the dashed line is the frequency band once the filter is applied.

specificities are addressed in the following paragraphs.

The sensor is an antenna with a main lobe of 30 to 45° depending on the considered setup. Since the expected radiation is unpolarized, there is no requirement on the polarization type of the antenna. The sensor is followed by an amplification and a filtering stage. The radio frequency signal is then transformed into a power envelope by a logarithmic amplifier (Analog Device AD8318) which delivers a voltage proportional to the logarithm of the RF input power. This model was chosen for its large frequency bandwidth and its fast time response of a few tens of ns. The output voltage is in turn adapted to the front end of the WCD electronics which is originally built to accept PMT's negative voltage between 0 and -2V (see Fig. 2). The adaptation is performed through an amplification that sets the dynamic range to 20 dB and an offset used to adjust the baseline level. The EASIER analogic signal replaces one of the six channels of the WCD front end electronics. The final part of the acquisition includes an antialiasing filter cutting frequencies above 20 MHz and the FADC (Flash Analog to Digital Converter) digitizer. The recorded waveform is 19.2 μ s long acquired with a 40 MS/s rate and has an amplitude sampled over 1024 ADC units (referred as ADCu in the following) [1]. The data stream is then sent to the central acquisition and the reconstruction of the EAS event is performed independently of the radio signals. As a consequence, no separate trigger for the radio signal is needed and the EASIER data are simply part of the regular SD data stream. As an additional benefit, the radio detector is powered by the station battery and is also integrated into the SD station monitoring system.

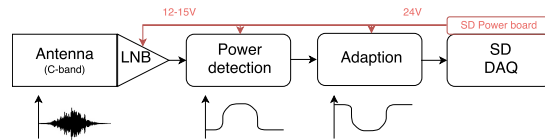


Figure 2: Block diagram of an EASIER detector unit.

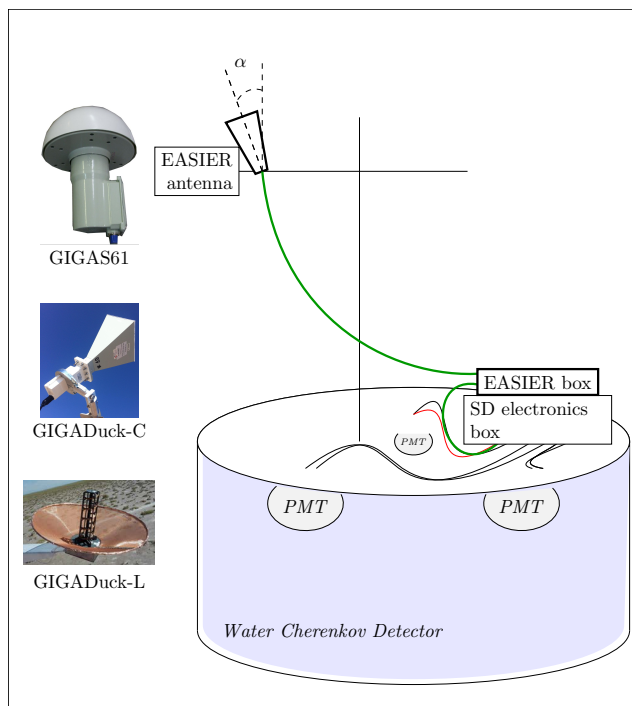


Figure 3: EASIER general scheme. One of the three antennas shown on the left hand side is installed on a pole that sits on the WCD. The antenna is vertical in the case of GIGAS61 and 6 out of 7 antennas are tilted by an angle $\alpha = 20^\circ$ in the GIGADuck hexagon design (see text). The RF signal is amplified and transferred to the GIGAS box to be transformed in its envelope and acquired in the SD acquisition.

GIGAS61

The GIGAS61 antenna is a commercial horn antenna (Fig. 3) made of a cylindrical feed and a quarter wave length monopole at its bottom. The metallic ring around the feed reduces the backlobe and widens the main lobe. A hemispherical radome is glued to the ring to protect the antenna from rain. The antenna has a gain of around 9 dB. It points to the Zenith and has a half-power beamwidth (HPBW) of 90° . It is tuned at a central frequency of 3.8 GHz and a bandwidth of approximately 500 MHz. It is associated with a low noise block (LNB) which amplifies the signal by approximately 60 dB and lowers down the central frequency to 1.35 GHz. The antenna and the LNB will be referred to LNBf hereafter. A bias tee is inserted after the LNBf to both distribute the power supply to the LNB and transmit the RF signal on a 75Ω line. The line impedance is adapted to 50Ω by a resistor bridge. The low-frequency part of the spectrum is filtered out by a 900 MHz high-pass filter. The adaptation electronics of GIGAS61 is made partly with commercially available device. The power detector used, the Minicircuit ZX47-50 is the encapsulated version of the Analog Device AD8318. The rest of the adaptation is carried out with a custom made board. A first array of seven detectors was installed at the Pierre Auger Observatory in April

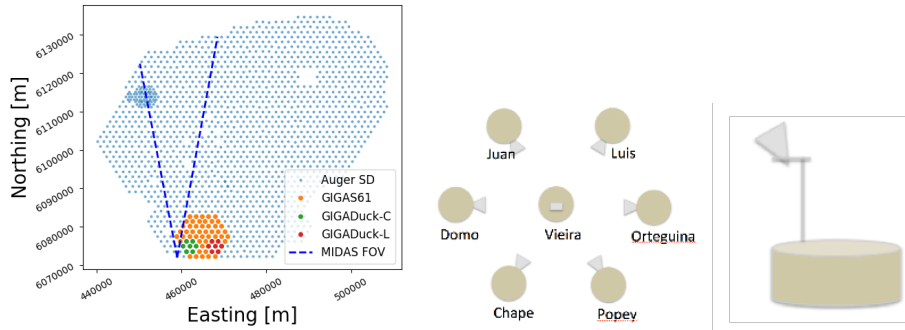


Figure 4: Left: GIGAS61, and GIGADuck arrays layout within the Pierre Auger SD. Middle and right: Top view of GIGADuck array and side view of one detector.

2011. The smooth operation and the results of this first test bed led to an extension by 54 more detectors covering a total instrumented surface of 93 km². The first seven LNBF are of the model GI301 made by Global Intersat and the 54 units of the extension are from WSInternational, model DMX241. The GIGAS61 array is located in the South-West part of the Pierre Auger Observatory. Its footprint is shown in Fig. 4-left. Even if the MBR signal is expected unpolarized, we fixed the polarization of each antenna. Out of the 61 antennas, 33 have a North-South polarization, and 28 an East-West one.

Several radio signals in the C-band were detected in coincidence with Auger EAS events with GIGAS61[15]. These detections validated the concept of the coincident radio detection and were the first detections of EAS in the C-band. However, such EAS emissions in the microwave band may have a different origin than MBR. In particular, the signals were detected at distances to the air shower axis of a few hundred meters only. This feature is in favor of the hypothesis of a beamed emission over an isotropic one as origin of these signals.

GIGADuck

The need to improve our sensitivity at large distance and to collect more data led to the design and installation of two optimized arrays, in the C-band and the L-band, with a higher antenna gain and a modified antenna orientation. The array is now composed of a central detector pointing to the Zenith with six peripheral detectors tilted by 20° in zenith and with azimuth adjusted to point towards the central detector (Fig. 4-middle and right). This configuration increases the overlap of the detectors field of view and enhance the probability to obtain a coincident detection. Indeed, this configuration was chosen because the observation of a coincidence between two radio detectors would support the hypothesis of an isotropic emission.

As an example of the improved performance of GIGADuck, the simulation of the radio signal power produced by MBR emitted by a vertical shower and detected by an antenna belonging either to GIGAS61 or to GIGADuck at a distance of 750 m is shown in Fig. 5. In the case of this particular configuration of distance and angle, the signal

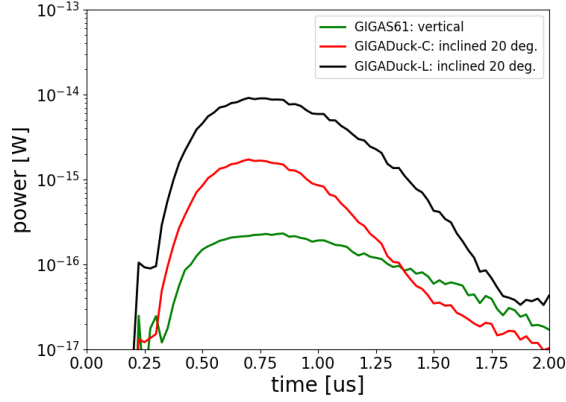


Figure 5: Simulation of the power received from a vertical 10 EeV shower as a function of time for GIGAS and GIGADuck-C detectors.

collected by the tilted GIGADuck-C antenna is around ten times larger, due mainly to the higher gain and the direction of the main lobe. In the L-band, the signal is increased by another factor 10, due to the quadratic dependence of the effective area of the antenna with the wavelength (see Eq. (2)). Further comparisons are shown in the section 4, they include calibrated value of detector noise and realistic distribution of the shower energies and arrival direction.

GIGADuck-C. In the C-band, the antenna is a pyramidal horn of 15 dB gain from the A-Info company. It increases the maximum antenna effective area by a factor of six with respect to the antennas of GIGAS61. It is protected by a thin radome in plexiglass. The LNB is a Norsat 8115F. It was chosen for its low noise figure and has a flatter response in frequency with respect to GIGAS61 horns, and thus a larger bandwidth.

GIGADuck-L. In the L-band, the sensor is a helicoidal antenna with a conical copper grid at its base. It is tuned to be sensitive to a central frequency of 1.4 GHz and a gain of 15 dB. The sensor is directly followed by an electric surge protection and a band-pass filter (from 1.1 to 1.4 GHz) to decrease the amplitude of the signal at 900 MHz caused by the GSM band and the SD communication system. The choice of placing a filter before the amplifier is not optimal in terms of noise figure but is necessary to prevent the amplifier saturation. The amplification board is composed of two separated amplifiers from the Avago company, the MGA633P8 and the MGA13116. They are combined to obtain a gain of around 50 dB. In both GIGADuck versions the adaptation electronics was made on custom made board with discrete components.

3. Detector calibration

EASIER detectors are required to measure faint and impulsive signals. The widely used figure of merit of the sensitivity for such detectors reads as

$$F = \frac{k_B T_{\text{sys}}}{A_{\text{eff}} \sqrt{\Delta\nu \Delta t}}, \quad (1)$$

where F represents the flux resulting from a signal that would equate the noise fluctuations, T_{sys} stands for the system noise equivalent temperature (the sum of the thermal noise collected by the antenna and the electronics noise added mainly by the first amplifier), k_B is the Boltzmann constant, A_{eff} is the effective area of the antenna (i.e. the portion of the incoming radio flux transformed into electrical power), and the square root term is the amount of samples over which the noise is averaged. In simple cases, $\Delta\nu \Delta t$ is the product of the bandwidth $\Delta\nu$ with a time constant of a low pass filter, but in cases of transient signals, the expected duration of the signals has to be used for Δt . We detail first the calibration of the sensor including the measurement or simulation of the parameters in Eq. (1). In a second time we determine the calibration parameters of the adaptation stage of the signal chain.

3.1. Sensor calibration

3.1.1. Antenna effective area

The effective area for a particular wavelength λ is derived from the knowledge of the antenna gain pattern $G(\theta, \phi)$, i.e. the gain of the antenna as a function of the direction:

$$A_{\text{eff}}(\theta, \phi) = \frac{\lambda^2 G(\theta, \phi)}{4\pi} \quad (2)$$

The gain pattern can be either measured or simulated. It has been measured for the antenna DMX241 from WS International and for an ATM horn coupled to a Norsat LNB in an anechoic chamber at the IMEP (Institut de Microelectronique Electromagnetisme et Photonique) at Grenoble. In addition to these measurements, the High Frequency Simulation Software (HFSS) from ANSYS [20] was used to simulate the patterns of the different antenna types, taking into account the setup of the sensors, such as the presence of a radome. The simulated effective area of the antenna used in the three setups are represented in Fig. 6.

3.1.2. System noise temperature

The system noise factor is defined as the degradation of the signal-to-noise ratio (SNR) along the signal chain stages and can be expressed with a system noise temperature, T_{sys} . The main contributions to the noise temperature are:

- the antenna temperature T_{ant} : the thermal noise emitted by broad microwave sources such as the sky or the ground collected by the antenna;
- the electronics noise T_{elec} : the noise added by the electronics stage, usually dominated by the first stage of amplification.

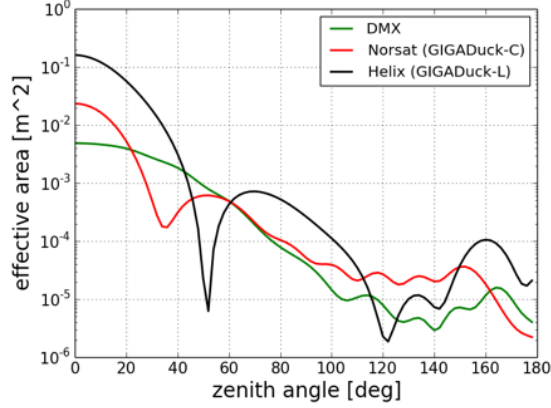


Figure 6: Simulated effective area for GIGAS61 (DMX), GIGADuck-C(Norsat) and GIGADuck-L (Helix) antennas.

A radome used to protect an antenna is a source of signal losses, affecting the SNR and adding up a contribution in the noise temperature.

To estimate the temperature of the three detector versions, we have applied three different methods. A well known method to measure a temperature contribution from a device like an amplification system is the Y factor method. It consists in the measurement of the device output when it is subject to two different known sources of noise. In the case of GIGAS61 and GIGADuck-C detectors, the amplification system is part of the feed and cannot be isolated and tested separately. Hence, to apply the Y factor method and produce a stable noise in the detector, the source has to be a microwave emitting source that covers most of the antenna main lobe. Having two references allows one to cancel out the gain of the system and to extract the noise. Another method is to make use of a natural microwave source like the Sun as a calibration source when it goes through the field of view of the antenna. Lastly, one can also directly measure the background radio power and deduce the noise temperature provided a precise knowledge of the system gain. The Y factor method was used in a dedicated measurement to obtain GIGAS61 detector temperatures. The second method is used for the GIGADuck arrays by measuring the Sun flux in the monitoring data. As it will be described later, the Sun signal was also used to correct for the pointing direction of GIGADuck-C antennas. Finally the direct method is used to measure the L-band setup system noise temperature.

GIGAS61 –. For GIGAS61 detectors, we apply the Y factor method to measure the electronics noise temperature. The measurement took place at the detector site. The setup comprises the main components of the nominal detectors, namely the LNBF, the radome and the power detector Minicircuit ZX47-50. The antenna was oriented consecutively up and down and the voltage of the power detector was recorded with a portable oscilloscope. The voltage difference between the two measurements is related

to a difference of power according to the calibration curve of the power detector (see Eq ((8)) in section 3.2.1). The electronics noise temperature T_{elec} is computed with:

$$T_{\text{elec}} = \frac{T_{\text{hot}} - Y T_{\text{cold}}}{Y - 1}, \quad (3)$$

where $Y = P_{\text{hot}}/P_{\text{cold}}$, T_{hot} (T_{cold}) is the antenna temperature when the antenna points toward the ground (the sky) and P_{hot} (P_{cold}) are the corresponding powers. The antenna temperature is the brightness temperature of the surrounding sources weighted by the antenna gain:

$$T_{\text{ant}} = \int_{\theta=0}^{\theta=\pi} \int_{\phi=0}^{\phi=2\pi} T_{\text{B}}(\theta, \phi) G(\theta, \phi) \sin \theta d\theta d\phi \quad (4)$$

with $T_{\text{B}}(\theta)$ the brightness temperature in the direction θ . We applied the formula (4) with a brightness temperature profile (found in [21]) which ranges from 4 K in the sky direction to 270 K towards the ground. Antenna temperatures of $T_{\text{hot}} = 260$ K and $T_{\text{cold}} = 6$ K are obtained. It yields to electronics temperatures of $T_{\text{elec}}^{\text{GSI}} = (114 \pm 10)$ K and $T_{\text{elec}}^{\text{DMX}} = (97 \pm 9)$ K. Finally we add the antenna temperature $T_{\text{ant}} = T_{\text{cold}} = 6$ K to obtain the system noise temperature.

GIGADuck-C -. Compared to GIGAS61 detectors, GIGADuck antennas have a larger effective area which make them sensitive to the Sun flux. Since GIGADuck data are part of the SD data stream including the monitoring system, the radio baseline is recorded every 400 s with other information such as the outside temperature. We use these data to search for the Sun signal and estimate the system temperature from it. The position of the Sun in the sky is well known and the absolute flux density in the frequency band is based on observations at the Nobeyama Radio Observatory (NRO) at 3.75 GHz ¹. Examples of the Sun path through the GIGADuck C-band array are shown in Figure 7. Most of the antennas (except the antenna on the stations called Juan and Luis) have the Sun passing through their field of view during the austral summer. However, when the Sun is low in the sky (during austral winter time), none of the antennas is sensitive to it. Since all GIGADuck antennas point in a different direction, one expects the Sun to produce a signal with relatively different intensity and shifted time of maximum according to their orientation. Indeed, we use both information to constrain together the system noise temperature and the pointing direction of the GIGADuck antenna.

The increase of power P_{Sun} induced upon the passage of the Sun over the system noise power P_{sys} in the antenna field of view reads

$$\Delta P [\text{dBm}] = 10 \log_{10} \left(\frac{P_{\text{sys}} + P_{\text{Sun}}(\theta_{\text{Sun}}, \phi_{\text{Sun}})}{P_{\text{sys}}} \right) = 10 \log_{10} \left(1 + \frac{1}{2} \frac{F_{\text{Sun}} A_{\text{eff}}(\theta_{\text{Sun}}, \phi_{\text{Sun}})}{k_{\text{B}} T_{\text{sys}}} \right), \quad (5)$$

where F_{Sun} is the total solar flux measured by the Nobeyama Radio Observatory [22] at 3.75 GHz, $A_{\text{eff}}(\theta_{\text{Sun}}, \phi_{\text{Sun}})$ is the antenna effective area for the given position of the Sun in the sky, and the factor 1/2 is the polarization factor. The radio baseline is strongly

¹The Nobeyama Radio Polarimeters are operated by Nobeyama Radio Observatory, a branch of National Astronomical Observatory of Japan

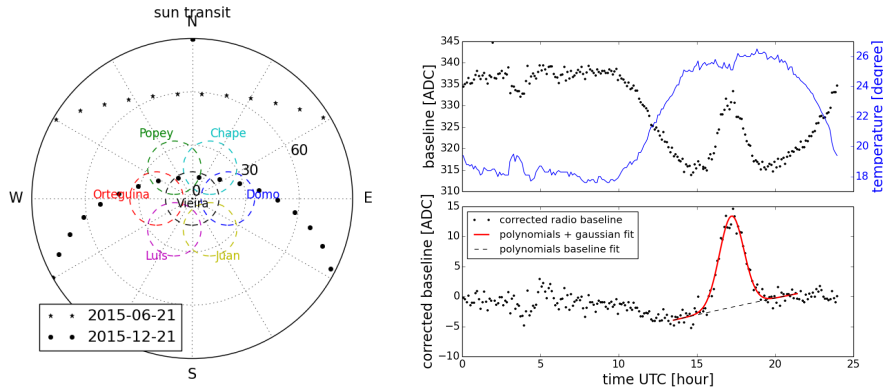


Figure 7: Left: Sun transit for the two solstices in polar coordinates where the radial distance represents the zenith angle. The azimuth is set to 0 for the East direction. The colored circles represent the field of view of the GIGADuck antennas. Right: Example of the baseline during one day. The top plot shows the original baseline and the outside temperature along the day. The bottom plot shows the baseline once corrected from the temperature dependence. The fit result is also shown in red.

correlated to the outside temperature, but can also be affected by the humidity in a non trivial way. We first operate a selection on the dataset to isolate a set of stable days, i.e. the days when the baseline is not affected by other parameters but the outside temperature.

Firstly, a time window of 8 hours around the time when the Sun is expected to produce the highest signal is removed temporarily. Then we reject the singular days when the baseline RMS is lower than 2 ADCu (compared to 20 ADCu typically). These low variations indicate that the signal chain was faulty at that time. Days with large amplitude, often due to thunderstorm condition, are removed by requiring baseline differences over the day lower than 200 ADCu. From this data set, the dependence of the radio baseline with the outside temperature is fitted with a linear function. To improve the selection of stable days, the day with the largest residual is removed and the fitting procedure is repeated until no residual larger than 10 ADCu is found. Then, the time window which encompasses the Sun contribution is restored in the selected days and the complete baselines are corrected for the temperature dependence. The final step consists in fitting the bump induced by the Sun flux with a Gaussian function and a third order polynomial. An example of the radio baseline is shown in Figure 7-right before the temperature correction (top) and after (bottom).

The selection and fit procedure are tested by introducing fake signals to mimic the Sun contribution in the real baselines of the antennas oriented towards the South (Luis and Juan) thus insensitive to the Sun. Signals with a Gaussian shape are introduced with various amplitude and time and are reconstructed according to the method described above. The uncertainty due to the limited knowledge of the baseline amounts to ± 4 ADCu on the amplitude of the peak and to ± 12 minutes on the time of maximum. The spread of the result of the fit is found to be ± 5 ADCu and ± 6 minutes.

Table 1: Results of fits, superscript and subscript are the statistical and systematics uncertainty respectively.

station name	Popey	Orteguina	Domo
original orientation θ/ϕ	20 / 120	20 / 180	20 / 0
new orientation $\theta_{\text{sys}}^{\text{stat}}, \phi_{\text{sys}}^{\text{stat}}$	$25_{+1/-1}^{+1/-1} / 116_{+1/-2}^{+1/-1}$	$23_{+3/-2}^{+1/-1}, 170_{+1/-1}^{+1/-1}$	$33_{+1/-1}^{+1/-1}, 12_{+6/-5}^{+5/-5}$
System Temperature $T_{\text{sys}}^{\text{stat}}$	$61_{+12/-10}^{+2/-2}$	$54_{+12/-7}^{+2/-1}$	$58_{+8/-9}^{+2/-3}$

The goal is to find the best parameters to describe the system noise temperature and the pointing direction given the observed amplitude and time of maximum. We simulate the signal induced by the Sun microwave flux for a system temperature from 30 to 120 K with 1 K step and for angles $\Delta\theta \in [0^\circ; 20^\circ]$ and $\Delta\phi \in [0^\circ; 180^\circ]$ around the nominal angle for the set of days selected in the aforementioned procedure. For each set of input parameters $(T_{\text{sys}}, \Delta\theta, \Delta\phi)$, the baselines in ADCu are computed. The best parameters are found by minimizing the following χ^2 :

$$\chi^2(T_{\text{sys}})|_{\Delta\theta, \Delta\phi} = \sum_i \frac{(t.o.m.i.\text{sim} - t.o.m.i.\text{data})^2}{\sigma_{t.o.m}^2} + \frac{(B_{i,\text{sim}} - B_{i,\text{data}})^2}{\sigma_B^2} \quad (6)$$

where each day is labeled with the index i , $t.o.m.$ stands for the time of the maximum in data and simulation, $B_{i,\text{data}}$ is the maximum of the fitted signal in ADCu in the data and $B_{i,\text{sim}}$ the signal in the simulation taken at the time of the maximum measured in the data (see the scheme in Figure 8-left). The result are given in the table 1. Angular deviations from the nominal position are found to be at most 14° (in angular distance) and temperatures range from 54 K to 61 K. An example of the temperature measured for each day in the data set and the time of maximum compared to the simulated one is shown in Figure 8-right.

GIGADuck-L-. The L-band sensors are also sensitive to the Solar flux. Thirty daily baselines are overlaid in Fig. 9 and exhibits the Sun passage (around 18 h) but also other modulation (for instance around 0 h or 7 h). These modulations, whose origin may be the positioning satellite signal, prevent us from quantifying the Sun contributions in the same way as above. Hence, the noise temperature is deduced from the direct measurement of the baseline, simply by dividing the measured power by the total gain of the system. This method requires a precise calibration of the absolute gain of the detector which was performed prior to the installation. The amplifier is pre-terminated and its gain and noise temperature could be measured respectively with a Vector Network Analyser and a Noise figure meter. In the C-band this measurement is made difficult by the use of LNBf and the impossibility to disconnect the amplification stage from the feed waveguide. The system noise temperature is measured for all seven L-band detectors, it ranges from 94 K to 145 K.

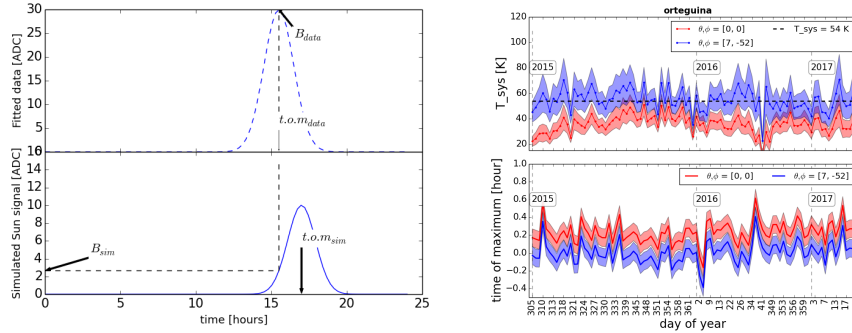


Figure 8: Left: Scheme with the parameters used in the χ^2 function in (6). Right: Temperature measured for one GIGADuck detector (Orteguina) with the Sun signal and time of maximum. We show together the results for the nominal antenna orientation (in red) and the one retrieved from the Sun observations (in blue).

3.1.3. Sensor bandwidth

The absolute gain of the RF part which includes the amplifier, the bias tee, the cables etc., does not enter directly in the detector sensitivity, but the frequency bandwidth does (see Eq. (1)). The normalized gains of the LNB used for GIGAS61 (DMX241) and GIGADuck-C and the GIGADuck-L are represented in Fig. 9 and the effective bandwidth is computed according to:

$$\Delta\nu = \frac{1}{G_{\max}} \int G(f)df \quad (7)$$

The obtained effective bandwidths for GIGAS61 detectors are 437 ± 30 MHz and 445 ± 56 MHz for the GI301 and the DMX241 respectively. As for the GIGADuck-C, a bandwidth of 750 MHz is measured for the Norsat LNB, and finally an average of 250 MHz is found for the GIGADuck-L LNAs.

3.2. Electronics calibration

We describe here the functioning of the adaptation electronics. The first part of this section is dedicated to the study of steady signal of the adaptation needed to describe the baseline level, while the second part describes the time response, necessary to simulate the full signal chain.

3.2.1. Response to steady signals

The adaptation electronics is composed of the power detector and the adaptation board. The power detector output voltage V_{pd} was calibrated in laboratory using a noise waveform. The noise was produced using the output of an actual LNBf placed in front of a microwave absorber to obtain the same spectrum as in the data. The input power P_{in} was varied with attenuators. The power-voltage characteristic reads:

$$V_{pd}[\text{V}] = -0.0234P_{in}[\text{dBm}] + \text{offset}_1, \quad (8)$$

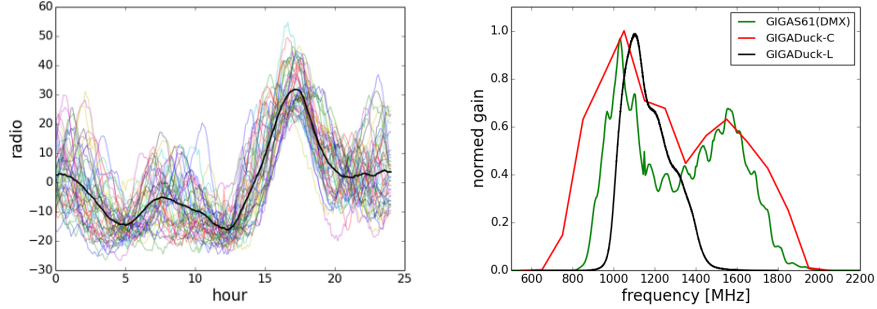


Figure 9: Left: 30 daily baselines for Jorge detector (GIGADuck-L). Right: Normalized gain of the three mentioned LNBF after the frequency downconversion. The thick blue and green lines are the average over several detectors. Only one measurement was performed with the Norsat LNBF (in red).

offset_1 is the voltage offset of the power detector. The power detector voltage is then amplified by a factor 4.2 to obtain a final power dynamics of 20 dB over the 2 V swing of the SD acquisition. An offset was designed to be adjustable on the adaptation board to make up for the differences of the detector gains. The overall conversion from the input power to the ADCu is:

$$P[\text{ADCu}] = 50.2P_{\text{in}}[\text{dBm}] + \text{offset}_2, \quad (9)$$

where offset_2 accounts for the total offset.

3.2.2. Response to impulsive signal

Power detector – To understand the power detector response to impulsive signals, we set a detection chain in the laboratory composed of a LNBF followed by a power detector. An impulsive and high frequency (HF) signal is produced by the spark of an electronic lighter. The signal is recorded simultaneously after the LNBF and after the power detector by a fast oscilloscope. An example of these signals is shown in Fig. 10. We can therefore build a method to reproduce the power detector output from a HF signal. We find that the power detector output is well reproduced when one performs the convolution of the HF signal in dBm (logarithmic unit) and an exponential function with a decay constant τ :

$$V_{\text{PD}}(t) = k_1 \int_{t>0} P_{\text{dBm}}(u) \exp\left(\frac{t-u}{\tau}\right) du + k_2 \quad (10)$$

The factor k_1 is fixed to the conversion factor in Eq. (8), k_2 is a floating offset and $\tau = 6.3 \text{ ns}$ was found to provide the best fit to the data.²

²The first seven detectors of GIGAS61 have a longer time response $\tau_{\text{capa}} = 41.5 \text{ ns}$ due to an output capacitor present by default in the power detector ZX47-50 and removed in the following version of EASIER.

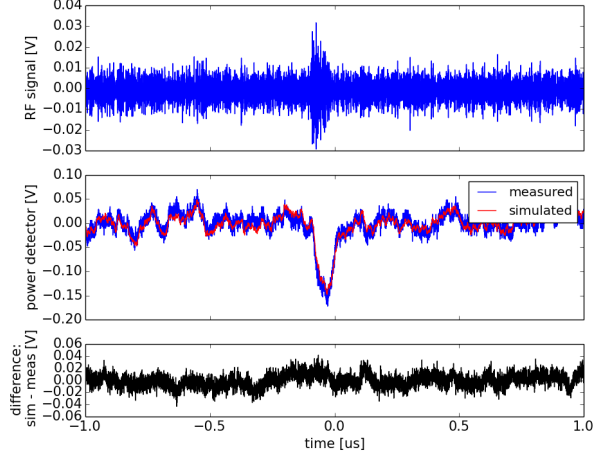


Figure 10: Example of RF and power detector waveforms. The top panel shows the RF waveform, the middle panel the waveforms after the power detector: the blue one is a measurement and the red is simulated from the waveform on the top panel. The lower panel show the difference of the power detector waveforms.

Adaptation board – To measure the response of the adaptation board, we add it to the calibration setup described in the previous paragraph. We recorded simultaneously the input of the board and its output. We find the board response by measuring the transfer function $\tilde{H}(f)$ in the frequency domain:

$$\tilde{H}(f) = \frac{\tilde{V}_{\text{out}}(f)}{\tilde{V}_{\text{in}}(f)}. \quad (11)$$

The gain and the phase of the board are represented in Fig. 11. The time response is obtained by Fourier transformation.

The last part of the chain, the Auger SD front end, is simulated with a low-pass filter with $f_{\text{cut}} = 20\text{MHz}$ and by sampling in time and amplitude.

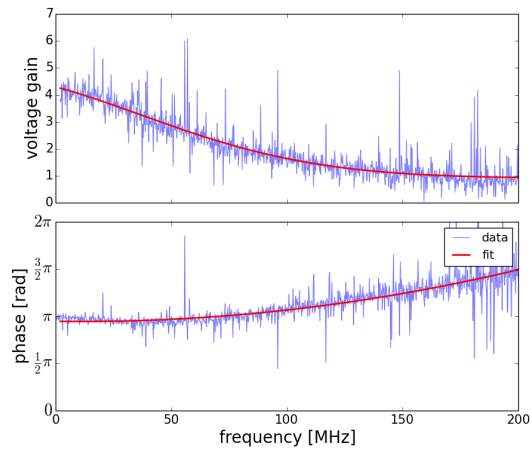


Figure 11: Measurement and fit of the gain and phase of the adaptation board.

4. Expected performances

This section is dedicated to presenting the performances of GIGAS61 and GIGADuck detectors in terms of EAS detection. In the section 4.1 we detail the method we implemented to estimate the flux from an EAS. In the section 4.2 we apply this method to estimate the expected number of events in one year of operation of GIGAS61 and GIGADuck detectors.

4.1. Simulation of the MBR signal from EAS

The longitudinal profile of EAS is parameterised with a Gaisser-Hillas function [23] characterising the number of charged particles at a certain depth. The mean values and RMS of the parameters used in the Gaisser-Hillas function are first tabulated for energies between $10^{17.5}$ and 10^{21} eV. A randomisation is then performed when generating an event using a Gaussian function for all the parameters except for the depth of first interaction which follows an exponential distribution. Starting from the first interaction point, high in the atmosphere, the number of primary electrons is calculated in grammage steps of $\Delta X = 2.5 \text{ g cm}^{-2}$. At each step, the mean energy deposit per particle is calculated following a parameterisation at 1 MeV given in [24]. The lateral distribution function of the electrons in the plane orthogonal to the shower axis is taken as an NKG function [25, 26].

The estimation of the flux of MBR photons emitted by the ionisation electrons and received at ground is based on the derivation presented in [19]. It accounts for the MBR differential cross section obtained in [27] and the time evolution of the shower plasma as the ionisation electrons get attached or see their energy shifted as they undergo ionisation or excitation reaction. The flux folded with the antenna effective area and integrated over the frequency bandwidth yields the power envelope of the signal as a function of the time at the receiver (an example of the power envelope is shown in Figure 12-left). Following the model in [19] we find a spectral intensity of $2 \times 10^{-26} \text{ W m}^{-2} \text{ Hz}^{-1}$ for a shower of $10^{17.5}$ eV observed at 10 km. This estimation allows for the comparison with other MBR studies. For instance, the same reference shower in the same conditions would produce a spectral intensity of $2.77 \times 10^{-24} \text{ W m}^{-2} \text{ Hz}^{-1}$ according to the results of SLAC T471 [10], the original beam test. We introduce a scale factor R based on the comparison of the reference shower, with $R = 1$ for the model that we used and $R = 140$ for the SLAC T471 assumption. The parameter R is used in the next section to assess the performance of the detectors.

To account for the detector response, the voltage deduced from the power envelope is multiplied with a noise waveform produced according to the spectra measured and presented in section 3.1. The resulting waveform is the simulation of the RF voltage induced at the output of the antenna by the EAS. A noise waveform is produced with the same spectrum, but the average power is normalized with the system noise temperature. We add the two waveforms to emulate the total RF voltage. The adaptation electronics is then simulated as described in section 3.2.2 to obtain a waveform in ADCu.

4.2. Expected event rate

For a scale factor R , the number of expected events for a time period ΔT and for an area labeled S inside which the shower core position is x, y reads as:

$$\mu(R) = J_0 \int_{>E_0} dE f(E) \int_{\Delta\Omega} d\Omega \cos\theta \int_S dx dy \int_{\Delta T} dt \varepsilon(E, \theta, \phi, x, y; R), \quad (12)$$

where ε , the detection efficiency, is estimated with the simulations described below. The energy E of the shower is generated randomly following the energy spectrum in the range above the so-called ankle energy which can be parameterised between $E_0 = 4 \times 10^{18}$ eV and 3×10^{20} eV according to [28]:

$$J(E; E > E_0) = J_0 f(E) = J_0 E^{-\gamma_2} \left(1 + \exp\left(\frac{\log_{10} E - \log_{10} E_{1/2}}{\log_{10} W_c}\right) \right)^{-1}, \quad (13)$$

where J_0 is a flux normalisation factor and the spectral index above the ankle γ_2 is 2.63. The term $\log_{10} E_{1/2}$ is the energy at which the flux has dropped to half of its peak value before suppression, and $\log_{10} W_c$ is its associated steepness. They are fixed to 19.63 and 0.15 respectively.

Shower cores are randomly generated over a surface covering an Auger hexagon, while the arrival directions θ and ϕ are randomly generated to guarantee uniformity in terms of ϕ and $\sin^2 \theta$ (with θ limited to 60°). For the three detectors, GIGAS61, GIGADuck-C and GIGADuck-L, we simulate 5000 proton showers. For each shower we compute the MBR power at the seven antennas of the hexagon. Scale factors R from 1 to 1000 are applied and the electronics is then simulated ten times for each R . The radio waveform is transformed in SNR unit according to: $P[\text{SNR}] = \frac{P - \langle P \rangle}{\text{RMS}(P)}$ (see Fig. 12-left). We apply simple selection criteria on these processed data. We select events with a waveform that passes a threshold of $\text{SNR} = 5$ in a time window of $1 \mu\text{s}$ around the expected time of maximum. The expected number of events for one equipped hexagon within a year of data taking is shown in Figure 12-right, where the abscissa axis is the scale factor. The initial implementation, GIGAS61, is already sensitive to the level of intensity as measured by SLAC T471 ($R = 140$) but would observe only one or two events. For the same scale factor, this number increases by a factor of 3 with GIGADuck-C. The best performances are obtained with GIGADuck-L with possible detection down to scale factor of around $R = 10$.

Several improvements in the analysis would help to identify MBR and are worth noting here. The basic event selection can be improved using digital filtering. Such analysis will particularly enhance the long duration signal (a few μs) as expected for MBR signal. Furthermore, in contrast to the geosynchrotron emission or the Askaryan effect, also present at GHz frequencies, the MBR emission is isotropic, this gives the possibility to identify it by requesting that the GHz radiation is detected at large distances. A plausible selection criteria would thus be performed on the number of stations that detected a radio signal in coincidence with the same shower. By requesting at least two stations spaced on the regular SD array (1500 m spacing), one would discard emissions arising from geosynchrotron or Askaryan effects (the expected signals of which expand over a few hundred meters only). Indeed, the antenna orientation of GIGADuck antennas was chosen optimized the coincidence probability.

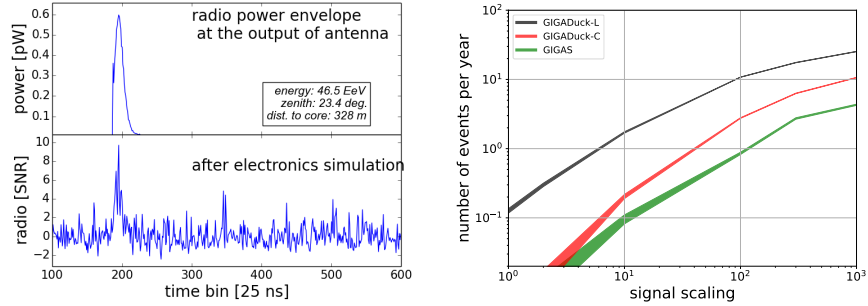


Figure 12: Left: Example of a simulated radio signal at the output of the antenna for a scale factor of 10, and when combined with the full electronics simulation. Right: expectation of the number of events per hexagon per year as a function of the MBR scale factor. The factor for SLAC T471 is $R=140$ (with $R=1$ corresponding to [19]).

However, even with these methods, if the MBR intensity is at the level of the reference model [19], its detection with the presented instruments is hardly possible with only 0.1 event expected per hexagon per year at best. To improve further the signal to noise ratio, other experimental techniques, like cryo-cooled detectors, should be considered. Note that the estimation of the MBR flux is delicate and if numerous processes are already included in [19] the conclusions on theoretical predictions are uncertain justifying the experimental prospection being carried out with GIGAS61 and the GIGADuck detectors.

5. Conclusion

GIGAS61 and its successors GIGADuck-C and GIGADuck-L are designed for the detection of MBR produced by EAS in the microwave frequencies and integrated in a Pierre Auger Observatory surface detector. This design was proven to be efficient since GHz signals associated to air showers were observed with the first implemented array GIGAS61. However the origin of such signal could not be attributed unambiguously to the MBR and detectors with an enhanced sensitivity (GIGADuck-C and GIGADuck-L) were installed.

We have demonstrated the good operation of the installed detectors and we performed a calibration of the parameters useful to describe their sensitivities, namely the effective area, the noise temperature and the bandwidth. The simulation of the electronics, and especially the response to short pulses was also studied and shown to be well understood.

The performance of these detectors was examined under various assumptions for the MBR intensity, and with a simulation of the detector chain. We verified the improvement of performance obtained with the GIGADuck detectors. For the most sensitive array (GIGADuck-L), the number of expected events is of the order of 15 per year for one equipped Auger hexagon when the original estimation from SLAC T471 is assumed. While the expectation from the most recent model of MBR emission is still be out of reach, GIGAS61 and GIGADuck detectors is able to probe *in situ* the flux of MBR over two frequency bands.

The detectors have been operating and accumulating data since 2011 for the first one and since end of 2016 for the last installed one. The analysis of the data to search for MBR signals or derive upperlimits on the intensity are being now carried out and will be presented in a future paper.

Acknowledgement

We gratefully acknowledge the very fruitful exchanges we had with all of our colleagues in the Auger collaboration and the use of all Auger facilities from hardware to software including access to a subset of shower data. We are also deeply indebted to the commitment of the observatory staff whose strong support in constructing and deploying the LSD prototype was extremely appreciated

We acknowledge the support of the French Agence Nationale de la Recherche (ANR) under reference ANR-12- BS05-0005-01.

References

- [1] A. Aab, et al., The Pierre Auger Cosmic Ray Observatory, Nucl. Instrum. Meth. A798 (2015) 172–213. [arXiv:1502.01323](#), [doi:10.1016/j.nima.2015.06.058](#).
- [2] The Telescope Array, Nuclear Physics B - Proceedings Supplements 125-126 (2008) 221–226.
- [3] M. Fukushima, Measurement of Ultra-High Energy Cosmic Rays: An Experimental Summary and Prospects, EPJ Web Conf. 53 (2013) 02002. [arXiv:1302.5893](#), [doi:10.1051/epjconf/20135302002](#).
- [4] J. V. Jelley, J. H. Fruin, N. A. Porter, F. G. Weekes, R. A. Porter, Nature 205 (1965) 327.
- [5] D. Ardouin, et al., Radioelectric Field Features of Extensive Air Showers Observed with CODALEMA, Astropart. Phys. 26 (2006) 341–350. [arXiv:astro-ph/0608550](#), [doi:10.1016/j.astropartphys.2006.07.002](#).
- [6] W. D. Apel, et al., Experimental evidence for the sensitivity of the air-shower radio signal to the longitudinal shower development, prd 85 (7) (2012) 071101. [arXiv:1203.3971](#), [doi:10.1103/PhysRevD.85.071101](#).
- [7] A. Aab, et al., Energy Estimation of Cosmic Rays with the Engineering Radio Array of the Pierre Auger Observatory, Phys. Rev. D93 (12) (2016) 122005. [arXiv:1508.04267](#), [doi:10.1103/PhysRevD.93.122005](#).
- [8] T. Huege, Radio detection of cosmic ray air showers in the digital era, Phys. Rept. 620 (2016) 1–52. [arXiv:1601.07426](#), [doi:10.1016/j.physrep.2016.02.001](#).
- [9] A. Aab, et al., Probing the radio emission from air showers with polarization measurements, Phys.Rev. D89 (5) (2014) 052002. [arXiv:1402.3677](#), [doi:10.1103/PhysRevD.89.052002](#).
- [10] P. Gorham, N. Lehtinen, G. Varner, J. Beatty, A. Connolly, et al., Observations of Microwave Continuum Emission from Air Shower Plasmas, Phys.Rev. D78 (2008) 032007. [arXiv:0705.2589](#), [doi:10.1103/PhysRevD.78.032007](#).
- [11] J. Alvarez-Muñiz, et al., The Air Microwave Yield (AMY) experiment - A laboratory measurement of the microwave emission from extensive air showers, PoS EPS-HEP2013 (2013) 026. [arXiv:1310.4662](#).
- [12] M. Monasor, et al., The Microwave Air Yield Beam Experiment (MAYBE): Measurement of GHz radiation for Ultra-High Energy Cosmic Rays detection, in: Proceedings,32nd International Cosmic Ray Conference (ICRC 2011): Beijing, China, August 11-18, 2011, Vol. 3, 2011, pp. 196–199, [3,196(2011)]. [arXiv:1108.6321](#), [doi:10.7529/ICRC2011/V03/0917](#).

- [13] J. Alvarez-Muñiz, et al., The MIDAS telescope for microwave detection of ultra-high energy cosmic rays, *Nuclear Instruments and Methods in Physics Research A* 719 (2013) 70–80. [arXiv:1208.2734](https://arxiv.org/abs/1208.2734), [doi:10.1016/j.nima.2013.03.030](https://doi.org/10.1016/j.nima.2013.03.030).
- [14] R. Smida, et al., First Experimental Characterization of Microwave Emission from Cosmic Ray Air Showers, *Phys. Rev. Lett.* 113 (22) (2014) 221101. [arXiv:1410.8291](https://arxiv.org/abs/1410.8291), [doi:10.1103/PhysRevLett.113.221101](https://doi.org/10.1103/PhysRevLett.113.221101).
- [15] R. Gaior, Detection of cosmic rays using microwave radiation at the Pierre Auger Observatory, in: *Proceedings, 33rd International Cosmic Ray Conference (ICRC2013): Rio de Janeiro, Brazil, July 2-9, 2013*, p. 0883.
- [16] K. Greisen, *Phys. Rev. Lett.* 16 (1966) 748.
- [17] G. Zapsetin, V. Kuzmin, *Sov. Phys. JETP Lett.* 4 (1966) 78.
- [18] I. Al Samarai, O. Deligny, D. Lebrun, A. Letessier-Selvon, F. Salamida, An Estimate of the Spectral Intensity Expected from the Molecular Bremsstrahlung Radiation in Extensive Air Showers, *Astropart. Phys.* 67 (26).
- [19] I. Al Samarai, C. Bérat, O. Deligny, A. Letessier-Selvon, F. Montanet, M. Settimo, P. Stassi, Molecular Bremsstrahlung Radiation at GHz Frequencies in Air, *Phys. Rev. D* 93 (5) (2016) 052004. [arXiv:1601.00551](https://arxiv.org/abs/1601.00551), [doi:10.1103/PhysRevD.93.052004](https://doi.org/10.1103/PhysRevD.93.052004).
- [20] HFSS, Ansys [®] Academic Research, Release 15.0.
- [21] T. Y. Otoshi, “Noise Temperature Theory and Applications for Deep Space Communications Antenna Systems“, Artech House, 2008.
- [22] [\[link\]](#).
URL <http://solar.nro.nao.ac.jp/norp/index.html>
- [23] T. Gaisser, A. Hillas, The Microwave Air Yield Beam Experiment (MAYBE): Measurement of GHz radiation for Ultra-High Energy Cosmic Rays detection, in: *Proceedings, 15th International Cosmic Ray Conference (ICRC1977): Plovdiv, Bulgaria, 1977, Vol. 8, 1977*, p. 353.
- [24] F. Nerling, J. Bluemer, R. Engel, M. Risse, Universality of electron distributions in high-energy air showers: Description of Cherenkov light production, *Astropart. Phys.* 24 (2006) 421. [arXiv:0506729](https://arxiv.org/abs/0506729).
- [25] K. Greisen, *Ann. Rev. Nucl. Sci.* 10 (1960) 63.
- [26] K. Kamata, J. Nishimura, *Prog. Theoret. Phys. Suppl.* 6 (1958) 93.
- [27] V. Kas’yanov, A. Starostin, On the Theory of Bremsstrahlung of Slow Electrons on Atoms, *Soviet Journal of Experimental and Theoretical Physics* 21 (1965) 193.
- [28] A. Schulz, et al., The measurement of the energy spectrum of cosmic rays above 3×10^{17} eV with the Pierre Auger Observatory, in: *Proceedings, 33rd International Cosmic Ray Conference (ICRC 2013): Rio, Brasil, 2013*. [arXiv:1307.5059](https://arxiv.org/abs/1307.5059).